YALE PEABODY MUSEUM

P.O. BOX 208118 | NEW HAVEN CT 06520-8118 USA | PEABODY.YALE. EDU

JOURNAL OF MARINE RESEARCH

The *Journal of Marine Research,* one of the oldest journals in American marine science, published important peer-reviewed original research on a broad array of topics in physical, biological, and chemical oceanography vital to the academic oceanographic community in the long and rich tradition of the Sears Foundation for Marine Research at Yale University.

An archive of all issues from 1937 to 2021 (Volume 1–79) are available through EliScholar, a digital platform for scholarly publishing provided by Yale University Library at https://elischolar.library.yale.edu/.

Requests for permission to clear rights for use of this content should be directed to the authors, their estates, or other representatives. The *Journal of Marine Research* has no contact information beyond the affiliations listed in the published articles. We ask that you provide attribution to the *Journal of Marine Research.*

Yale University provides access to these materials for educational and research purposes only. Copyright or other proprietary rights to content contained in this document may be held by individuals or entities other than, or in addition to, Yale University. You are solely responsible for determining the ownership of the copyright, and for obtaining permission for your intended use. Yale University makes no warranty that your distribution, reproduction, or other use of these materials will not infringe the rights of third parties.

A note on evanescent behavior of Arctic thermohaline intrusions

by David Walsh[1] and Eddy Carmack[2]

ABSTRACT

Temperature/salinity interleaving is a signature of thermohaline transition in the Arctic Ocean. These interleaving features, or "intrusions," are observed to decrease in amplitude as they spread laterally from warmer toward cooler water. Here this phenomenon is investigated by considering the effect of a nonlinear equation of state on intrusion structure and behavior. The analysis shows that large-scale gradients of the thermal expansion coefficient (α) can induce a spatial decay of intrusion temperature, salinity, and velocity amplitudes toward cooler water. Spatial decay implies a recirculating flow between adjacent layers, which induces a slow vertical propagation of the intrusions. The temperature-dependence of α provides a mechanism which may act to trap intrusions in the vicinity of warm Arctic boundary currents, inhibiting ventilation of cooler waters.

1. Introduction

Climate change in the Arctic has received a great deal of attention recently, with evidence documenting retreat of Arctic ice cover in recent decades (Rothrock *et al.,* 1999), a weakening of the Arctic halocline (Steele and Boyd, 1998), and warming in the Canadian Basin (Carmack *et al.,* 1995). Some of these changes may be related to fluctuations in warm Atlantic water inflow which are advected through the Arctic Basin by narrow, topographically steered boundary currents. It is unclear how such signals of climate change are communicated to basin interiors, and so the mechanisms responsible for the warming observed by Carmack *et al.* (1995) and others are not known. During the 1994 Arctic Ocean Section (AOS94) expedition, Swift *et al.* (1997) observed an extensive array of thermohaline intrusions, which are shown by the fine-scale temperature fluctuations in Figure 1. The intrusions appear to originate in topographically steered boundary currents, and to decay with distance away from their source regions (Fig. 2). It is possible that the intrusions provide a mechanism for transmission of climate-change signals at intermediate depths.

The Arctic intrusions were found to be very uniform in scale, with a vertical extent of around 40 m close to the Atlantic layer core, and were remarkably coherent in temperature/

---

1. International Arctic Research Center, University of Alaska Fairbanks, P.O. Box 75-7335, Fairbanks, Alaska, 99775-7335. U.S.A. *email: david.walsh@iarc.uaf.edu*
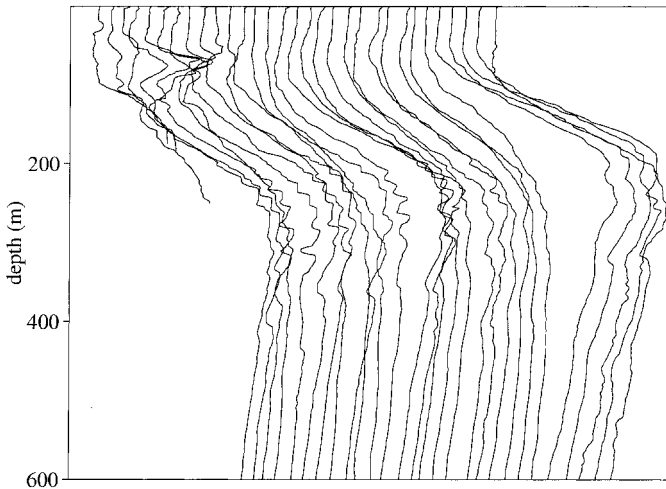2. Institute of Ocean Sciences, 9860 W. Saanich Road, Sidney, BC, Canada, V8L 4B2.

Figure 1. Temperature profiles from the AOS94 cruise (stations 5–35), extending from the Chukchi Slope to the Lomonosov Ridge, showing strong intrusive activity in the vicinity of the Atlantic water layer. Maximum temperatures of $\approx 1.5°C$ are found close to 200 m; surface temperatures are approximately $-1.6°C$.

salinity (T-S) space. They are likely long-lived, as similar T-S structures were observed during the *Henry Larsen* cruise in 1993 (Carmack *et al.,* 1995), and during cruises in the Eurasian Basin in both 1991 and 1996 (Rudels *et al.,* 1999). Furthermore, remarkably similar structures were observed in the Eurasian Basin as long ago as 1981 (Perkin and Lewis, 1984). CTD data from the AOS94 cruise show that the intrusions have a cusped or saw-tooth character in T-S space (Fig. 3a), and widely separated profiles are closely aligned in T-S space, demonstrating coherence over distances greater than 2000 km. The intrusions migrate downward across density surfaces as they spread from warmer to cooler water (Fig. 3a), suggestive of active mixing and buoyancy fluxes between interleaving layers. It is remarkable that T-S slopes within profiles are so similar, both in finger (warm + salty over cool + fresh) and diffusively stratified (cool + fresh over warm + salty) portions of the water column. The lining-up ("nesting") of finger-stratified layers evident in Figure 3 shows that vertical T-S variations are precisely matched to lateral T-S variations, suggesting that large-scale lateral variation within the Atlantic layer strongly influences local vertical gradients (cf. Iselin, 1939).

Carmack *et al.* (1998) speculated that the extensive interleaving features observed by Swift *et al.* (1997) played a role in the recent warming at mid-depths, and thus are an important mechanism by which the Arctic Ocean responds to fluctuations in warm Atlantic water inflow. Based on the assumption that they were responsible for the recent warming, Carmack *et al.* (1997) estimated the effective lateral diffusivity for the intrusions to be very large, of order 3000 m^2 s^{-1}. In contrast, the Joyce (1977) model (based on an assumed local balance between advective production of T-S variance and dissipation by vertical
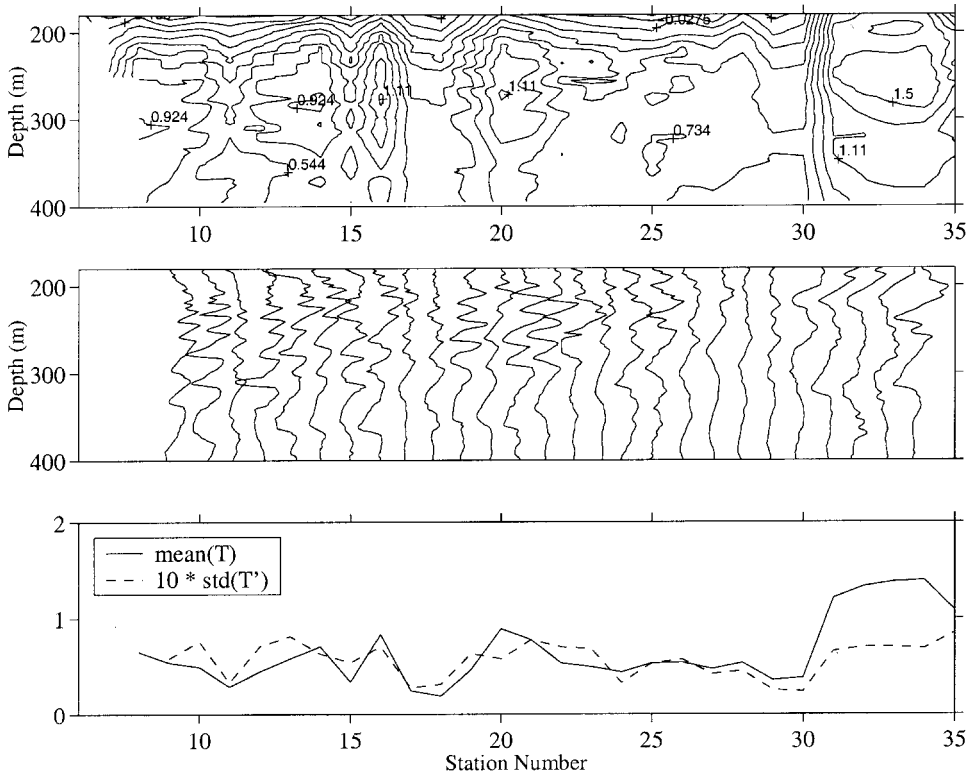
Figure 2. A temperature section from the AOS94 data (top panel), showing currents flowing along the Alpha-Mendeleev and Lomonosov ridges. The middle panel shows high-pass-filtered temperature anomalies and strong intrusive signatures along the boundaries of the ridge currents (the largest anomalies have peak-to-peak amplitudes of nearly 0.5°C). The bottom panel shows depth-averaged temperature (solid curve) and standard deviation of temperature anomaly (a measure of intrusion amplitude) for the data shown in the upper panels.

mixing) gives the independent estimate $K_h = K_v T_z^2 / \bar{T}_x^2 \approx 200 \text{ m}^2 \text{ s}^{-1}$, using $K_v \approx 3 \times 10^{-5} \text{ m}^2 \text{ s}^{-1}$, $T_z \approx 0.5°\text{C}/20 \text{ m}$, and $\bar{T}_x \approx 1°\text{C}/100 \text{ km}$ (where K_v is an estimate of the effective diapycnal diffusivity[3] for temperature, T_x is the large-scale horizontal temperature gradient, and T_z the fine-scale temperature gradient associated with intrusions). The computed value for K_h is smaller than the estimate of Carmack *et al.*, but still suggests the intrusions are an effective lateral mixing mechanism [a value of $1000 \text{ m}^2 \text{ s}^{-1}$ being typical of mixing by mesoscale eddies in the North Atlantic (Freeland *et al.*, 1975)].

Intrusion amplitudes decay toward lower temperatures, both vertically and horizontally (Figs. 3a,b), becoming quite small at temperatures below about 0.5°C. Thus, while Arctic

---

3. This value is taken from Ruddick and Hebert's (1988) analysis of data from a Mediterranean salt lens, and is slightly larger than the value of $\sim 10^{-5} \text{ m}^2 \text{ s}^{-1}$ predicted by Kelley's (1984) empirical formula.
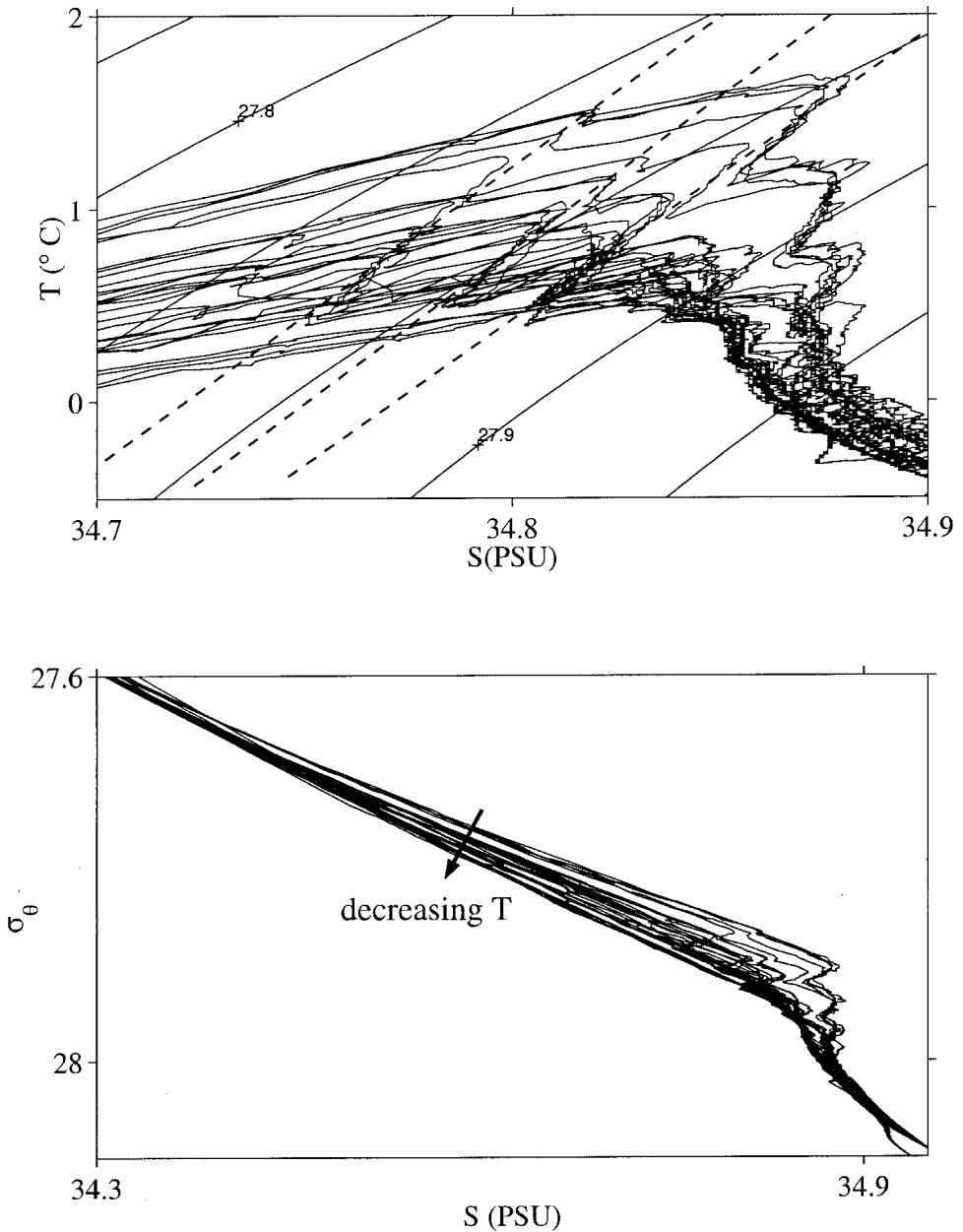
Figure 3. *T-S* plot (panel a) showing AOS94 data and strong intrusive activity near the core of the Atlantic water layer. Cusps are the signature of intrusions; contours show σ_t lines. Note the tendency for the curves to line up along a series of lines in *T-S* space, demonstrating a high degree of lateral coherence. Dashed lines show least-squares best-fits for three of these lines, with a mean slope of 15.4°C · PSU^{-1}. Panel b shows the data plotted in $S - \sigma_\theta$ space, showing that density becomes increasingly a function of S alone at lower temperatures.

interleaving structures are extensive, they appear incapable of penetrating the coldest parts of the Arctic Basin. The spatial nature of the decay can be seen in Figure 2 (panels b + c), where amplitudes are seen to decay away from warm ridge-trapped currents. Spatial decay in intrusion amplitude has also been noted by Rudels (1999, his Fig. 10). Lateral variation of intrusion amplitude and its relation to temperature is shown in Figure 4, in which intrusion amplitude for the depth range 160 m–500 m is plotted versus maximum Atlantic layer temperature. Amplitudes appear roughly constant at temperatures above ~0.7°C, and there is a clear tendency for amplitudes to decrease with temperature below ~0.7°C. A similar behavior is apparent in Figure 4b, which plots RMS amplitude versus average temperature for the full data set, using 120 m depth-bins. Each point represents the standard deviation of T for a 120 m segment, plotted against the mean T for that segment. The similarity with Figure 4a suggests that the factors causing lateral variation in intrusion amplitude may also be responsible for the observed vertical decay. Data for which $\sigma_\theta >$ 27.89 (dark symbols) exhibit a pattern different from that for data with $\sigma_\theta <$27.89: deeper intrusions appear to vanish at temperatures below ~0.4°C, while at shallower depths they persist to lower temperatures (~0°C).

There are several possible explanations for the observed decrease in amplitude. First, the intrusions may not have sufficient time to penetrate throughout the basin if Atlantic water inflow varies too rapidly. Second, intrusions may be trapped within high-lateral-gradient regions adjacent to boundary currents because they cannot generate the density anomalies essential to growth when they spread beyond these regions. This follows from consideration of the feedback loop which drives intrusions: (a) vertically sheared, quasi-lateral advection across a front produces small T-S anomalies at certain depths, (b) these anomalies lead to anomalous diapycnal buoyancy fluxes which reinforce the cross-front motion, (c) enhanced cross-front motion reinforces the original T-S anomalies closing the feedback loop. This feedback loop "works" as long as the effective diffusivities for T and S are different, and the initial displacement lies within a certain range of angles. When horizontal T-S gradients become too small the feedback is weakened, causing intrusions to decay away from frontal regions. This is fundamentally the mechanism investigated by Niino (1986).

In addition to the possibilities discussed above, the Arctic has a number of characteristics which deserve special consideration. As an example, nonlinearity in the equation of state (EOS) for seawater becomes more important at low temperatures, a consequence being that in cooler water a given temperature anomaly has a smaller density signature than it would in warmer water. This nonlinearity is manifested by curvature of density lines in the T-S plane (Fig. 3a); this curvature is larger at lower temperatures, and density lines are steeper. Because theory suggests the intrusions found above the Atlantic layer temperature maximum are primarily driven by buoyancy fluxes associated with destabilizing vertical temperature gradients, it is important to understand how they are affected by this nonlinearity as they spread toward cooler waters.

Here we investigate the possibility that nonlinearity in the equation of state exerts a
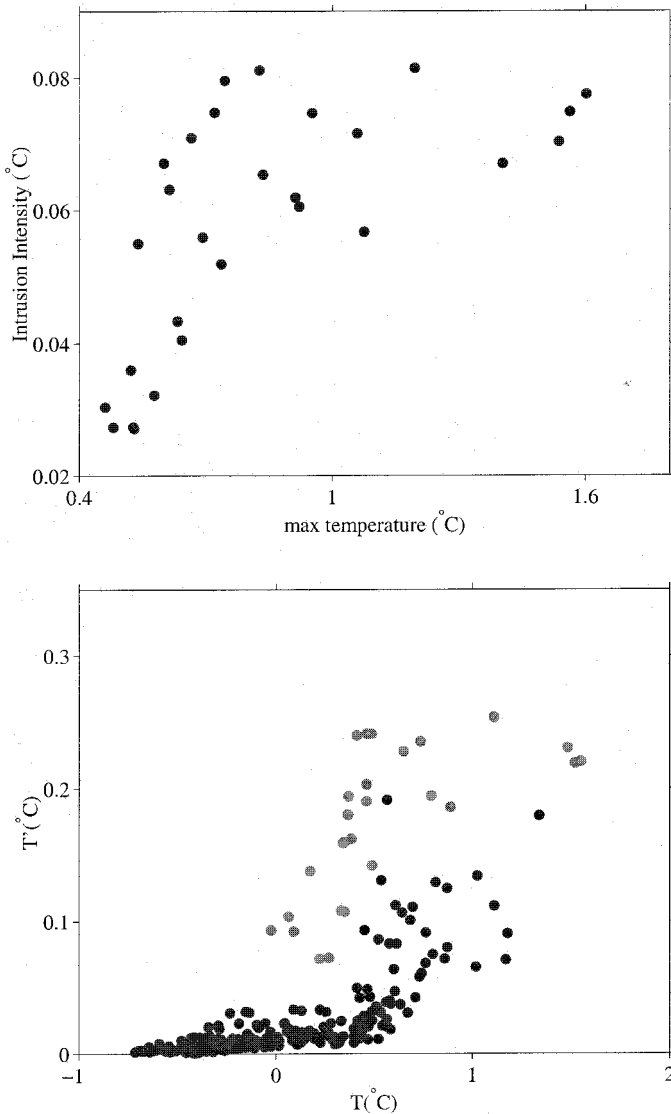
Figure 4. Temperature anomaly amplitude versus maximum Atlantic layer temperature (panel a), illustrating the tendency for intrusion amplitudes to decay toward cooler water. Panel b is similar to panel a, except that the data have been analyzed in 120 m depth bins, so both depth-variations and lateral variations should be apparent. Each point represents the standard deviation of T for a segment plotted against the mean T for that segment. Darker symbols show data with $\sigma_\theta > 27.89$; data with $\sigma_\theta < 27.89$ are shown by lighter symbols. The similarity with panel a suggests the mechanism causing vertical decay in amplitude is similar to that causing lateral decay.

regulating influence on intrusion amplitudes, perhaps contributing to the observed spatial decay. The study will focus on the behavior of the intrusions in the diffusively stratified region above the core of the Atlantic water layer, considering what happens when intrusions formed in relatively warm water spread toward cooler water. It will be shown using a simple model that this can lead to suppression of the intrusions. A primary motivation for this work is to discover whether there are mechanisms inherent to intrusion dynamics which can inhibit their spread and/or modify their amplitudes, and hence limit outward heat fluxes from boundary/ridge-trapped currents. The result may have implications for the heat budget of the Arctic Ocean, since the net oceanic heat flux into the basin depends on how efficiently Atlantic water mixes with surrounding waters.

2. Background

A number of well-understood mechanisms are available to explain aspects of Arctic intrusion behavior. Simple theoretical models of double-diffusively driven interleaving (e.g., Toole and Georgi, 1981) can help explain basic features such as vertical scales, slopes, and growth rates. These theories are typically based on linearized stability calculations, assuming intrusions to be infinite planar disturbances growing in a background with uniform horizontal and vertical gradients. Such theories typically do not address the evanescent behavior evident in the AOS data. Evanescent behavior is well known in many other contexts, an example being lateral trapping of water waves resulting from bathymetric variations. Little relevant theoretical work has been done relating to interleaving; a notable exception being found in the work of Niino (1986), who investigated a simple model of horizontally inhomogeneous interleaving, reconciling differences between the "wide-front" model of Toole and Georgi (1981) and the narrow-front model proposed by Ruddick and Turner (1979). In addition, Richards (1991) investigated lateral trapping of intrusions in the equatorial band resulting from variation of the Coriolis parameter with latitude. No work has been done to determine the effect on intrusions of the large temperature gradients bounding the Atlantic water layer. Given the prominence of these intrusions in the Arctic data, it is important to try to understand their dynamics and how they influence the evolution of larger-scale fields.

Nonlinear density effects are manifested in a number of ways, the most familiar being through cabbeling. Cabbeling is a consequence of the curvature of density lines in T-S space, and leads to a relative densification following mixing of water parcels with differing T-S values. Other examples are the thermobaric instability (Gill, 1973), which results from the pressure-dependence of the thermal expansion coefficient α, and the recent suggestion (Fofonoff, 1998) that nonlinearity may establish maximum allowable temperature gradients within the thermocline. The potential effect of nonlinearity can be seen by considering the stability parameters introduced by Fofonoff (1961), and discussed more recently by Fine *et al.* (1978) and Fofonoff (1998). These studies suggest cabbeling may be an important energy source for mixing

when gradients become large. In this work we focus on the linear stage when gradients are small and cabbeling effects presumably weak. Even in the absence of mixing, however, there may be small horizontal density gradients resulting from the temperature-dependence of the thermal expansion coefficient α. The influence of such gradients appears at the linear stage and can affect intrusion growth and evolution—the effect of these gradients on interleaving will be the focus of this study. Our approach is a departure from most previous interleaving studies, which take parameters such as α and β (the haline contraction coefficient) to be constant.

Nonlinearity in the equation of state is apparent in the curved density contours seen in Figure 3a, and the corresponding variation of α and β in the S-T plane can be seen in Figure 5. Variation of α is clearly the dominant nonlinearity, since α varies by a factor of two over the ranges of T and S shown, while β varies by only about 1%. The implication is that using a linearized equation of state is inappropriate over the ranges of T and S shown, and that, while β may reasonably be taken to be constant, α cannot. Figure 5a suggests that the nonlinearity can be modeled to a first approximation by a T-dependent thermal expansion coefficient $\alpha(T)$ over the ranges of T and S seen in the AOS94 data. We will show that this variation of α introduces new dynamics at low temperatures. Incorporating the effect leads to an additional term in the linearized equations governing the growth of small-amplitude intrusions, producing an asymmetry between warm (descending) and cool (ascending) intrusions, and consequent spatial variation in intrusion amplitude.

3. The model

a. Effect of α on density

We begin by considering how density anomalies which drive interleaving are affected by the nonlinear equation of state. Defining T_0 and S_0 to be the basic-state temperature and salinity at (x_0, z_0) and expanding the equation of state about (S_0, T_0) gives:

$$\rho(S, T) = \rho_0 \left[1 + \frac{\rho_T}{\rho_0}(T - T_0) + \frac{\rho_S}{\rho_0}(S - S_0) + \frac{\rho_{TT}}{2\rho_0}(T - T_0)^2 \right.$$
$$\left. + \frac{\rho_{ST}}{\rho_0}(S - S_0)(T - T_0) + \frac{\rho_{SS}}{2\rho_0}(S - S_0)^2 + \cdots \right], \tag{1}$$

where all derivatives are evaluated at (S_0, T_0) and we have ignored pressure effects for maximum simplicity. Introducing the standard notation

$$\alpha = -\frac{\rho_T}{\rho_0}$$
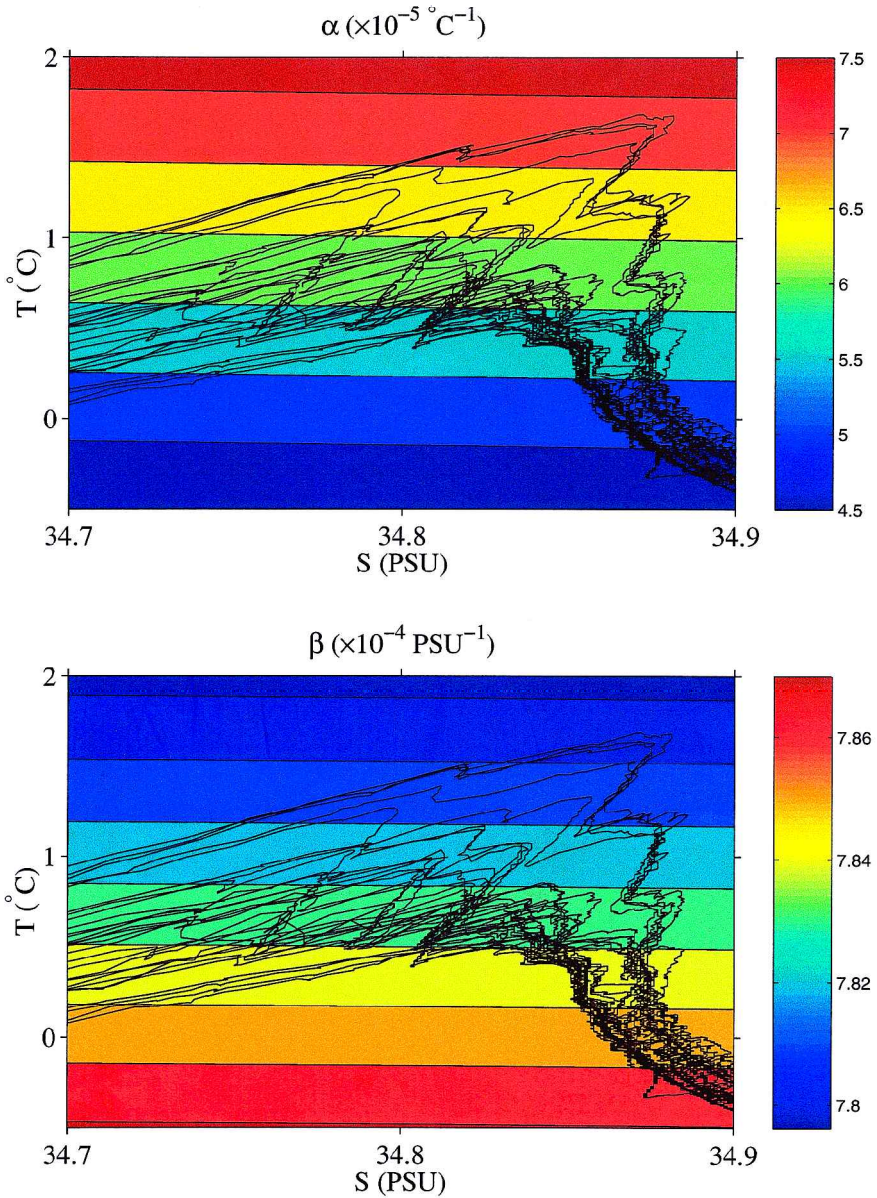
$$\beta = +\frac{\rho_S}{\rho_0}, \tag{2}$$

Figure 5. Variation of α (top) and β (bottom) in the *T-S* plane, with *T-S* data overlain. α varies by roughly 50% over the range of *T* and *S* shown in the plot while β varies by less than 1%, demonstrating that nonlinearity associated with α-variations dominates over that due to β-variation.

where α is the thermal expansion coefficient and β the haline contraction coefficient, gives

$$\rho(S, T) = \rho_0(1 + \beta^0(S - S_0) - \alpha^0(T - T_0) - \tfrac{1}{2}\alpha_T^0(T - T_0)^2 + \cdots), \tag{3}$$

where $\alpha^0 = \alpha(S_0, T_0)$, $\beta^0 = \beta(S_0, T_0)$, and the fact that β changes little over the relevant range of S and T has been used to justify neglect of terms containing derivatives of β. The ratio of the last two terms in (3) measures the importance of nonlinear density effects; for $T_0 = 0$ this ratio is of $O(1)$ when $T - T_0 \sim \alpha^0/\alpha_T^0 \sim 4°C$. This is similar to the range of temperatures seen in the AOS data, suggesting that nonlinear density effects are likely to be dynamically important.

The lateral density gradient which drives interleaving is given by:

$$\begin{aligned}
\rho_x &= \rho_S S_x + \rho_T T_x \\
&\approx \rho_S S_x - \rho_0(\alpha^0 + \alpha_T^0(T - T_0))T_x \\
&\approx \rho_0\underbrace{[\beta^0\bar{S}_x - \alpha^0\bar{T}_x]}_{\text{basic—state}} + \rho_0\underbrace{[\beta^0 S_x' - \alpha^0 T_x' - \boxed{\alpha_T^0\bar{T}_x T'}]}_{\text{perturbations}} + \cdots \\
&\equiv \bar{\rho}_x + \rho_x',
\end{aligned} \tag{4}$$

where $T = T_0 + \bar{T}(x, z) + T'(x, z, t)$, $S = S_0 + \bar{S}(x, z) + S'(x, z, t)$, and the scaling assumption $\alpha_T^0\bar{T}/\alpha^0 \ll 1$ has been used to justify neglect of terms containing $\alpha_T^0\bar{T}$. These scaling assumptions limit the validity of solutions to a finite range of x, and imply that, to this level of approximation, α may be considered constant unless differentiated. The boxed term represents the correlation between background temperature and α variations, describing the part of the perturbation density gradient resulting from horizontal gradients in α. This term introduces a dynamical asymmetry, causing density anomalies to be different for warm and cool anomalies of equal amplitude. Its form is consistent with a simple x-dependent formulation for α, in which case the perturbation density gradient can be written:

$$\rho_x' \approx \rho_0(\beta S_x' - (\alpha T')_x), \tag{5}$$

where

$$\alpha = \alpha^0 + \alpha_T^0\bar{T}_x x \tag{6}$$

is a simple linear function of x.

b. Model equations

The analysis will focus on a simplified set of equations corresponding to "model 1" of Toole and Georgi (1981), in which they consider the behavior of intrusions in a nonrotating system. It is assumed that the Prandtl number $Pr = A/K$ is large enough that the momentum balance is approximately steady, and it follows that the governing equations are:

Table 1. Estimated parameter values for the region above the Atlantic layer core (100–200 m).

Parameter	Description	Value
K	vertical eddy diffusivity	3×10^{-5} m^{2}s^{-1}
N^2	squared buoyancy frequency	3×10^{-5} s^{-2}
α	thermal expansion coefficient	6.6×10^{-5}°C^{-1}
β	haline contraction coefficient	7.8×10^{-4} PSU^{-1}
α_x	α gradient	$-(5 - 4) \times 10^{-5}$°C^{-1}/100 km $= \ldots$ $= -1 \times 10^{-10}$°C^{-1} m^{-1}
$\tilde{\alpha}_x$	dimensionless α gradient $\left(= \dfrac{\alpha_x}{\alpha_0} \sqrt{\dfrac{\overline{K}}{N}} \right)$	-1.8×10^{-7}
$\bar{T}_z$	vertical temperature gradient	-2°C/100 m $= -0.02$°C m^{-1}
$\tilde{T}_z$	dimensionless " $(= g\alpha \bar{T}_z /N^2)$	-0.26
$\bar{T}_x$	lateral temperature gradient	-1°C/100 km $= -1 \times 10^{-5}$°C m^{-1}
$\tilde{T}_x$	dimensionless " $(= g\alpha \bar{T}_x /N^2)$	-1.31×10^{-4}
$\bar{S}_z$	vertical salinity gradient	-0.5 PSU/100 m $= -0.005$ PSU m^{-1}
$\tilde{S}_z$	dimensionless " $(= g\beta \bar{S}_z /N^2)$	-1.27
$\bar{S}_x$	lateral salinity gradient	-0.05 PSU/100 km $= \ldots = -5 \times 10^{-7}$ PSU m^{-1}
$\tilde{S}_x$	dimensionless " $(= g\beta \bar{S}_x /N^2)$	-1.27×10^{-4}
m	dimensionless vert. wavenumber $\left(\approx \dfrac{2\pi}{40 \text{ m}} \sqrt{\dfrac{\overline{K}}{N}} \right)$	0.01

$$0 = -p_x/\rho_0 + Au_{zz}$$

$$0 = -p_z/\rho_0 - g\rho'/\rho_0$$

$$T_t + u\bar{T}_x + w\bar{T}_z = KT_{zz}$$

$$S_t + u\bar{S}_x + w\bar{S}_z = \gamma_d KT_{zz}\alpha/\beta \qquad (7)$$

$$u_x + w_z = 0$$

$$\rho' = \rho_0(\beta S' - \alpha(x)T'),$$

where α is assumed to be a linear function, as in (6). These equations govern the evolution of vertical and horizontal velocity components, temperature (or, more precisely, potential temperature), and salinity. The main difference between (7) and the system considered by Toole and Georgi (1981) is that here the thermal expansion coefficient α is not constant; this will result in spatial variations in intrusion amplitude associated with background temperature variations. Physically, the formulation has introduced a new length scale, a frontal scale-width L_α defined by $\alpha/\alpha_x (\approx 400$ km using values from Table 1), which represents the scale at which variations in α become dynamically important. We anticipate variation in model solutions at this scale.

Neglect of rotation can be justified in part by referring to the work of McDougall (1985), who showed that it caused the fastest-growing intrusions to tilt in the along-front direction, but did not otherwise affect the character of the fastest-growing disturbance. However, this justification is questionable in the presence of baroclinic shear (Zhurbas *et al.,* 1988; Kuz'mina and Rodionov, 1992; May and Kelley, 1997), which is almost always present at oceanic fronts. Such along-front shear will modify along-front slopes of intrusions, and may have a consequent effect on cross-front fluxes. Because of these considerations, we justify (7) as the simplest system which illustrates the physical mechanism of interest.

Interleaving is believed to be driven by buoyancy fluxes resulting from differing mixing rates for heat and salt, such as might be produced by diffusive convection, so fluxes in (7) are linked using a flux ratio γ:

$$F_T = -KT_z$$
$$\beta F_S = \gamma_d \alpha F_T. \tag{8}$$

Conceptually, we imagine these flux laws apply to a basic-state made up of small-scale double-diffusive steps and layers with vertical scales much smaller than an intrusion wavelength. *T-S* fluxes through these interfaces are assumed to drive the growth of small-amplitude intrusions. A basic state comprised of small-scale steps and layers is qualitatively in accord with observations, which show extensive small-scale *T-S* structure. The form of the flux laws is directly analogous to that proposed by Stern (1967) for the salt-finger case, although here it is written in a form suitable for diffusive-sense convection. If γ_d is less than one (we use the value of 0.15 suggested by Turner (1965)) diffusive convection can release potential energy available in the temperature field. No parameterization for salt-finger fluxes is given, since these calculations apply only to the small-amplitude stage, before salt-finger stratified layers form.

A velocity streamfunction ψ is introduced, defined by

$$w = \psi_x, \quad u = -\psi_z, \tag{9}$$

and temperature and salinity fields are written in the form

$$T = T_0 + \bar{T}(x, z) + T'(x, z, t)$$
$$S = S_0 + \bar{S}(x, z) + S'(x, z, t) \tag{10}$$
$$\psi = \psi',$$

where T_0 and S_0 are average values, $\bar{T}(x)$ and $\bar{S}(x)$ are large-scale, spatially varying background fields, and T' and S' represent intrusions. Assuming the intrusions have small amplitudes ($\nabla|T'| \ll |\nabla\bar{T}|$), (7) can be approximated by the linear system:

$$A\psi'_{zzzz} - g(\beta S'_x - \alpha T'_x - \alpha_x T') = 0$$
$$T'_t - \psi'_z \bar{T}_x + \psi'_x \bar{T}_z = KT'_{zz} \tag{11}$$
$$S'_t - \psi'_z \bar{S}_x + \psi'_x \bar{S}_z = \gamma_d KT'_{zz}\alpha/\beta,$$

where all parameters are considered constant to this degree of approximation, and isopycnals are assumed flat in the basic-state. Eq. (11a) expresses a steady vorticity balance in which lateral motions are driven by intrusion-generated horizontal density gradients.

c. *Spatial structure*

Solutions to (11) grow or decay with x when $\bar{\alpha}_x \neq 0$. This represents a mechanism for spatial trapping of intrusions, and differs from the constant-α case, where solutions have spatially uniform amplitudes. To demonstrate this we look for solutions to (11) of the form

$$(\psi', T', S') = \text{Real}[(\hat{\psi}(x), \hat{T}(x), \hat{S}(x))e^{imz+\lambda t}]. \tag{12}$$

If m and λ are real, this represents solutions which are oscillatory in depth, exponentially growing (or decaying) in time, with arbitrary x-dependence. This results in an equation for the horizontal structure of $\hat{\psi}$:

$$\hat{\psi}_{\tilde{x}\tilde{x}} + P\hat{\psi}_{\tilde{x}} + Q\hat{\psi} = 0$$

$$P \equiv -i\tilde{m}\,\frac{\tilde{S}_x(1 + \tilde{m}^2/\tilde{\lambda}) - \tilde{T}_x(1 + \gamma_d\tilde{m}^2/\tilde{\lambda}) - i\tilde{\alpha}_x\tilde{T}_z\tilde{m}^{-1}(1 + \gamma_d\tilde{m}^2/\tilde{\lambda})}{\tilde{S}_z(1 + \tilde{m}^2/\tilde{\lambda}) - \tilde{T}_z(1 + \gamma_d\tilde{m}^2/\tilde{\lambda}) - Pr\tilde{m}^2\tilde{\lambda}(1 + \tilde{m}^2/\tilde{\lambda})} \tag{13}$$

$$Q \equiv \tilde{m}^2\,\frac{Pr\tilde{m}^2\tilde{\lambda}(1 + \tilde{m}^2/\tilde{\lambda}) + i\tilde{\alpha}_x\tilde{T}_x\tilde{m}^{-1}(1 + \gamma_d\tilde{m}^2/\tilde{\lambda})}{\tilde{S}_z(1 + \tilde{m}^2/\tilde{\lambda}) - \tilde{T}_z(1 + \gamma_d\tilde{m}^2/\tilde{\lambda}) - Pr\tilde{m}^2\tilde{\lambda}(1 + \tilde{m}^2/\tilde{\lambda})},$$

where P and Q are functions of the dimensionless quantities

$$\tilde{x} = x\left(\frac{K}{N}\right)^{-1/2}$$

$$\tilde{m}^2 = m^2 K/N$$

$$\tilde{T}_x = g\,\frac{\alpha}{\alpha_0}\,\alpha_0\bar{T}_x/N^2$$

$$\tilde{S}_x = g\beta\bar{S}_x/N^2$$

$$\tilde{T}_z = g\,\frac{\alpha}{\alpha_0}\,\alpha_0\bar{T}_z/N^2 \tag{14}$$

$$\tilde{S}_z = g\beta\bar{S}_z/N^2$$

$$\tilde{\lambda} = \lambda/N$$

$$Pr = A/K$$

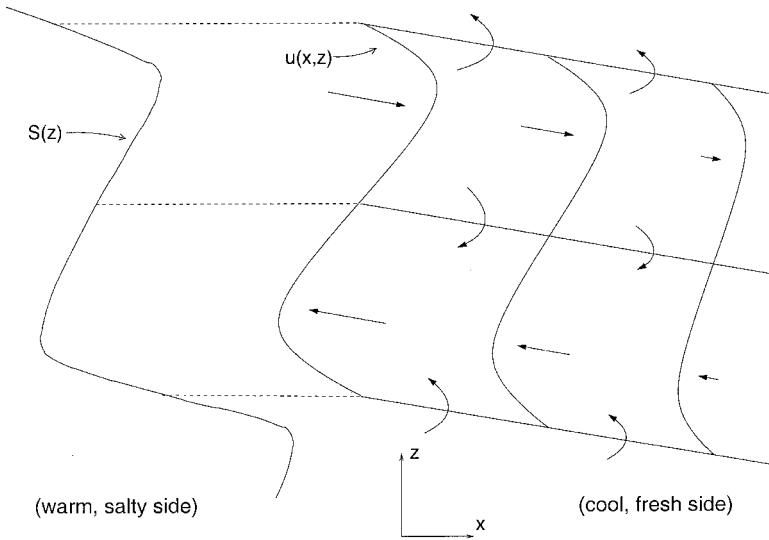$$\tilde{\alpha}_x = \frac{\alpha_x}{\alpha_0}\sqrt{\frac{K}{N}}$$

Figure 6. Schematic showing velocities associated with interleaving, decaying to the right, and the recirculating flow required by continuity. A typical salinity profile is shown to the left.

and the buoyancy frequency N is defined as

$$N = \left(-\frac{g}{\rho_0} \frac{\partial \rho}{\partial z} \right)^{1/2}. \tag{15}$$

In deriving (13) the simplifying assumption that x-variations occur on scales large compared to z-variations ($\partial/\partial \tilde{x} \ll \partial/\partial \tilde{z}$) has been made. This approximation should be strongly satisfied for the Arctic intrusions (which have slopes less than $\sim 10^{-4}$).

Solutions to (13) exist of the form $\hat{\psi} = e^{i\tilde{k}\tilde{x}}$, where $\tilde{k}$ is a root of

$$\tilde{k}^2 - iP(\tilde{m}, \tilde{\lambda})\tilde{k} - Q(\tilde{m}, \tilde{\lambda}) = 0, \tag{16}$$

and P and Q are complex, and defined as in (13). If $\tilde{\lambda}$ is real, roots of (16) are real (representing intrusions with uniform amplitude) when $\tilde{\alpha}_x = 0$, and are complex (representing sinusoidally modulated solutions which grow or decay in x) when $\tilde{\alpha}_x \neq 0$. The character of the evanescent solutions is shown in Figure 6. The behavior of the roots may be clarified by expressing the wavenumber in the form $\tilde{k} = \tilde{k}_r + i\tilde{k}_i$ and substituting into (16), which gives

$$\tilde{k}_i = \frac{\text{Im}Q + \tilde{k}_r \, \text{Re}P}{2\tilde{k}_r + \text{Im}P}. \tag{17}$$

Using the definitions of P and Q, Eq. (17) implies that $\tilde{k}_i = 0$ when $\tilde{\lambda}$ is real and $\tilde{\alpha}_x = 0$. In this case solutions are purely oscillatory in x, with uniform amplitude. However, if $\tilde{\lambda}_i = 0$

and $\tilde{\alpha}_x \neq 0$, $\tilde{k}_i$ is nonzero and of $O(10^{-7})$ for the parameter values listed in Table 1, representing a dimensional decay scale of some 1000 km. Evanescence results from positive feedback between decreased density anomalies and decreased cross-front velocities, leading to exponential trapping in space. In the marginally stable case (for which $\tilde{\lambda} = 0$) (17) becomes

$$k_i^* = L_\alpha^{-1} \cdot G(\tilde{k}_r, \tilde{m}, \tilde{S}_x, \tilde{T}_x, \tilde{S}_z, \tilde{T}_z)$$

$$G = \frac{\gamma_d}{\tilde{S}_z - \gamma_d \tilde{T}_z} \left(\frac{\tilde{T}_x/\tilde{m} - \tilde{k}_r \tilde{T}_z}{2\tilde{k}_r - \tilde{m} \dfrac{\tilde{S}_x - \gamma_d \tilde{T}_x}{\tilde{S}_z - \gamma_d \tilde{T}_z}} \right) \tag{18}$$

$$L_\alpha = \alpha/\alpha_x$$

in dimensional terms, demonstrating linear dependence on the scale width L_α.

The behavior of the roots is shown by contouring $\tilde{k}_i$ as a function of $\tilde{m}$ and $\tilde{\lambda}_r$ (Fig. 7): the case $\tilde{\alpha}_x = 0$ is shown in Figure 7a and Figure 7b shows the case $\tilde{\alpha}_x \neq 0$. Notice that when $\tilde{\alpha}_x = 0$ there are purely real wavenumbers representing "standard" intrusions as well as evanescent solutions; when $\tilde{\alpha}_x \neq 0$ all values of $\tilde{\lambda}$ and $\tilde{m}$ correspond to complex wavenumbers. In Section 3e the situation in which both $\tilde{\lambda}_i$ and $\tilde{k}_i$ are nonzero is discussed. For physical reasons solutions will be valid only when $\tilde{k}_i \ll \tilde{k}_r$, since if $\tilde{k}_i$ is too large (i.e., intrusion amplitude decays too rapidly) nose effects not considered in the present wide-front intrusion model may become important. Eq. (16) gives the controlling behavior of linearized intrusion solutions—the full leading-order asymptotic behavior may be obtained via WKB analysis (see the Appendix).

The decaying nature of solutions can be understood by considering T-S flux vectors driving intrusion growth at two different temperatures (Fig. 8). At higher temperatures the advective flux vector rises relative to isopycnals, and the resultant T-S vector ("res") has a relatively small density signature. When the intrusion moves into cooler water the advective flux vector becomes more nearly isopycnal (due to curvature of density lines), so the resultant has a larger cross-isopycnal component[4]. Hence, at lower temperatures density anomalies are larger for a fixed temperature anomaly. The situation shown illustrates the linear stage, before salt-finger interfaces form, but it may apply qualitatively at the nonlinear stage as well. Some support for this scenario may be obtained by considering the buoyancy budget of intrusions. Plotting σ_θ anomalies versus the corresponding temperature anomalies (Fig. 9) demonstrates that warm anomalies are relatively heavy, consistent with their sinking across density surfaces (anomalies are computed relative to the low-pass filtered temperature and salinity profiles). Data with segment-averaged temperature greater than 0.4°C are shown by dark symbols; data with average temperatures

---

4. The two sets of vectors in Figure 8 have been drawn parallel based on the observation (Fig. 3a) that intrusions follow near-straight-line trajectories through T-S space, rather than curving to follow density lines.
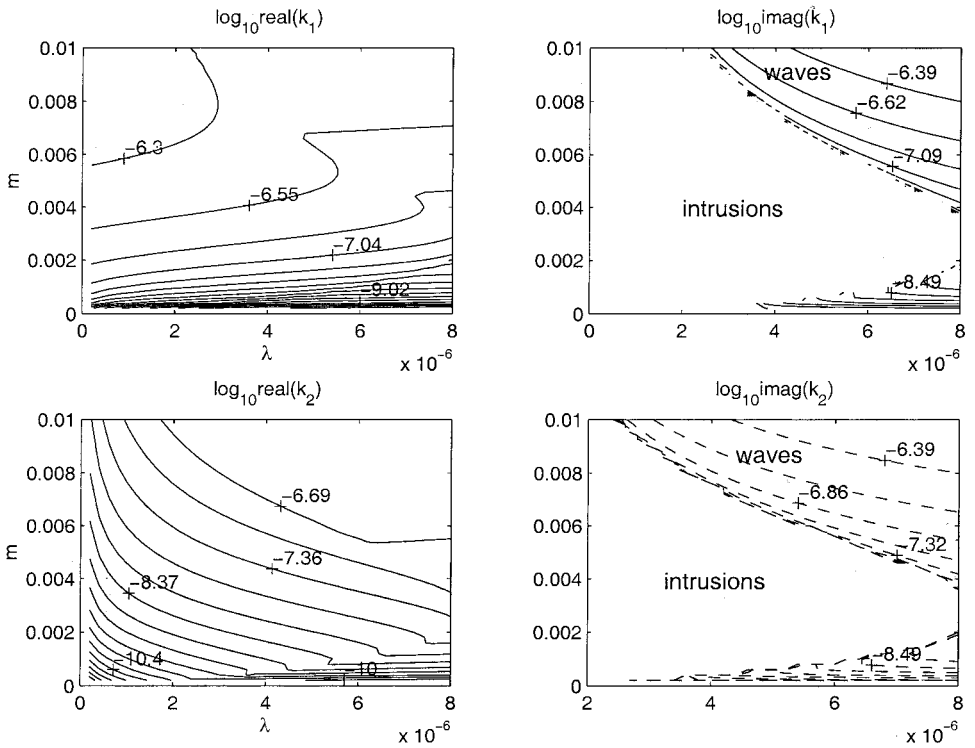
Figure 7. Logarithm of horizontal wavenumber $\tilde{k}$ as a function of vertical wavenumber $\tilde{m}$ and Real($\tilde{\lambda}$). The contour maps show the two solutions to (16), with the real part of $\tilde{k}$ shown to the left and the imaginary part to the right. Dashed contours show negative values. The first four panels show the roots for the nonevanescent case (note the area of purely real wavenumbers representing "standard" intrusions); the remaining four panels show roots for the evanescent case, in which case all wavenumbers are complex.

less than 0.4°C are shaded. The plot clearly shows an increase in slope for lower temperatures, suggesting that a given temperature anomaly corresponds to larger density anomaly at lower temperatures, in agreement with Figure 8. The apparent explanation for this is that temperature makes a larger relative contribution to the density signature of a warmer intrusion, so the density anomaly is smaller for a given size of temperature anomaly.

d. Nonlinear trapping mechanism

In the previous section the mechanism by which lateral gradients in α may lead to spatial decay of small-amplitude intrusions was described. Here the case in which intrusions reach large amplitude will be discussed with the goal of understanding whether there are absolute limits (e.g., critical temperatures) beyond which they can no longer grow. The arguments presented are speculative, based on dynamically plausible extrapolations from the linear
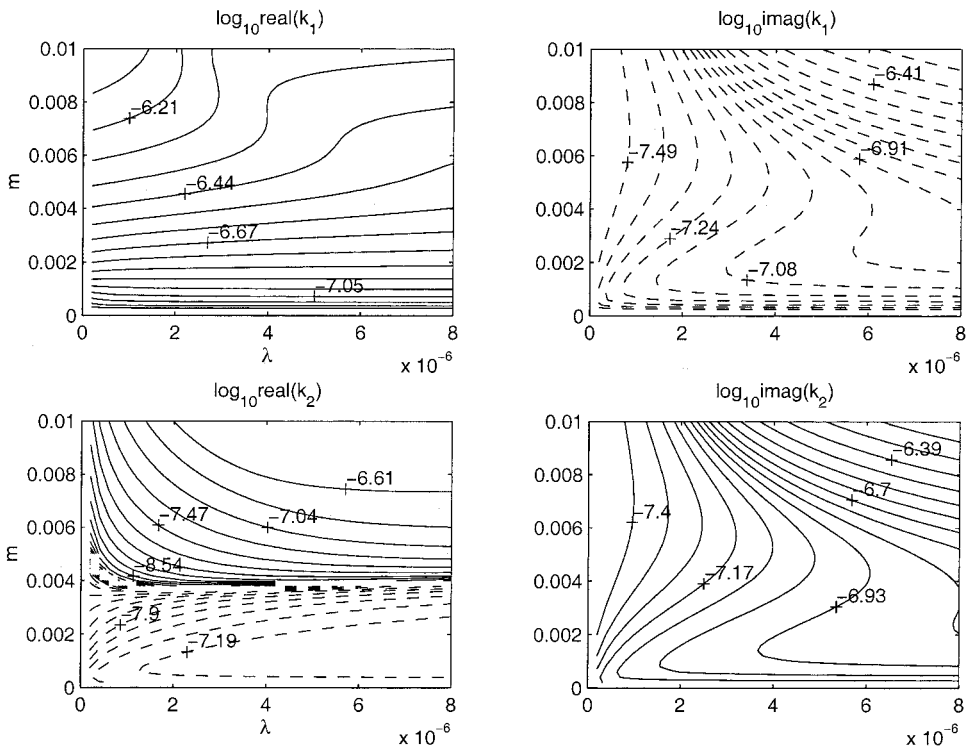
Figure 7. (Continued)

theory and inferrences from data, and we emphasize that they do not necessarily follow from the linear theory.

A limiting case of the trapping phenomenon is illustrated in Figure 10 for an intrusion spreading from warm to cool water. The lines along which intrusions move through T-S space (dashed line) appear straight, while density lines are concave-down. At sufficiently low temperatures these "trajectories" may become parallel to density lines, as at the lower-left corner of the plot, resulting in static instability. Notice that the effect is amplitude-dependent (see inset), occurring at higher temperatures for larger-amplitude intrusions. This amplitude dependence results from the downward concavity of density contour lines, which dictates that the average slope of a density line between T and $T + \Delta T$ is greater than that at T if $\Delta T < 0$ (as illustrated), and less if $\Delta T > 0$. The "nested" structure of the intrusions implies that when this critical temperature is reached, both horizontal and vertical density gradients vanish within finger layers. The above ideas may help explain the shrinkage of intrusion amplitude seen at lower temperatures (Fig. 3): as intrusions spread toward cooler water and stratification in finger layers decreases, vertical mixing increases, decreasing the extent of finger layers in T-S space. Mixing to homogeneity would reduce a layer to a single point, at which point the intrusions effectively become
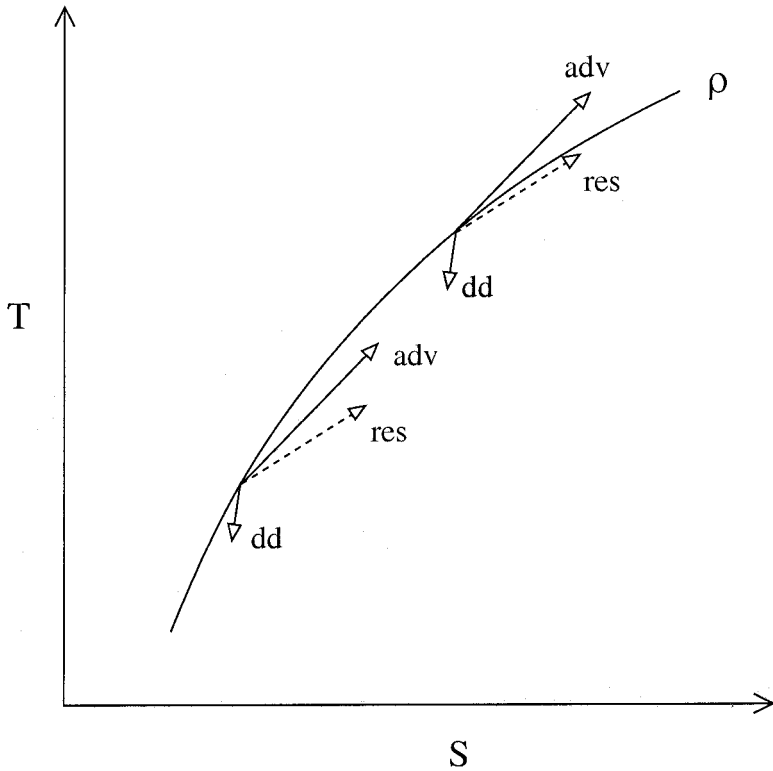
Figure 8. Illustration of the effect of nonlinearity on the density signature of growing, small-amplitude intrusions. The total T-S signature of an intrusion is the vector sum of a component due to advection ("adv") and another due to double-diffusive mixing ("d.d."). At lower temperatures the advective flux vector makes a larger angle with density lines, so density anomalies are larger for a fixed T-S disturbance amplitude.

staircases (this idea has been discussed by Merryfield (2000)). When intrusions reach this point of marginal stability other physical processes such as cabbeling may become important. Our speculation is that fluxes through salt-finger stratified layers are likely to be dominantly turbulent, since these layers are thick and relatively weakly stratified.

In Figure 11 the slope of density lines in T-S space (given by the ratio β/α) is plotted as a function of temperature (for $S = 34.85$ PSU and $P = 300$ dbar). The slope is a decreasing function of T, decreasing from ~16.5 at $T = -1°$C to ~11 at $T = +1°$C (solid curve). The thin horizontal line shows the mean slope of the dashed lines connecting finger layers in Figure 3—about 15.4°C PSU^{-1}. Notice that the two solid curves intersect close to $T = -0.75°$C, indicating intrusions cannot grow at temperatures lower than this. The dashed line shows the same situation for an intrusion with a peak-to-peak amplitude of 0.5°C [given by $(\delta T/\delta S)_{\rho = \text{const}} \approx (1 + \alpha_T T'/2\alpha)^{-1}\beta/\alpha$, from (3)]. Notice that the slope is larger because the *average* slope of a density line between temperatures T and $T - 0.5$ is
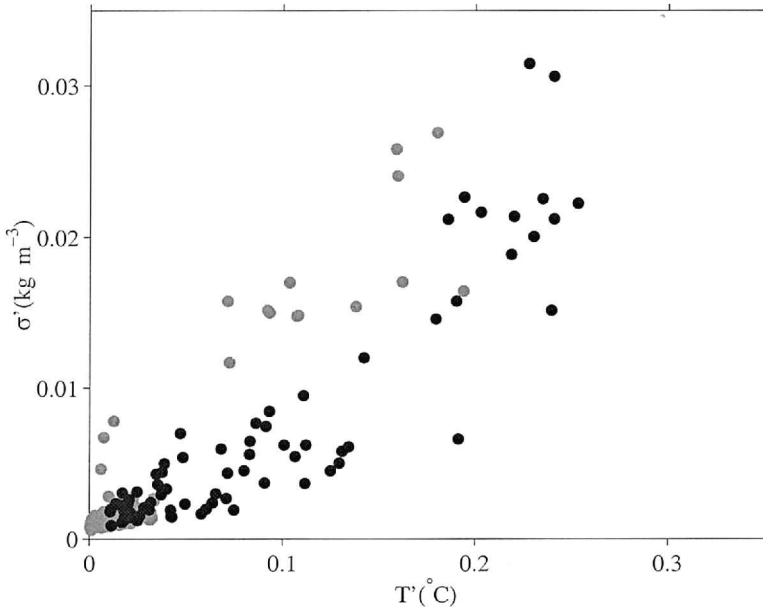
Figure 9. Correlation between T anomalies and σ_θ anomalies, demonstrating the tendency of warm anomalies to sink relative to density surfaces. Darker symbols show data with segment-averaged temperatures greater than 0.4°C; lighter symbols show data with segment-averaged temperatures less than 0.4°C.

greater than that at T (Fig. 10, inset). The dashed and thin lines intersect at $T \approx -0.5°C$, suggesting intrusions with this amplitude cannot grow at temperatures below about $T = -0.5°C$, in reasonably good agreement with behavior seen in the T-S plots. If these speculations are correct, this temperature may act as a boundary beyond which the intrusions are strongly inhibited—waters with temperature below this critical value would then be effectively shielded from penetration by intrusions.

e. Propagation

In this section the effect of evanescence on interleaving velocities is considered. Continuity requires the following relation between velocity components:

$$\frac{\hat{w}}{\hat{u}} = -\frac{\tilde{k}_r}{\tilde{m}} - i\frac{\tilde{k}_i}{\tilde{m}}$$

$$= -\left(\frac{\sqrt{\tilde{k}_r^2 + \tilde{k}_i^2}}{\tilde{m}}\right) e^{+i\tan^{-1}(\tilde{k}_i/\tilde{k}_r)} \tag{19}$$

showing there is a phase-shift between horizontal and vertical velocities. The size of the phase-shift is measured by $\tilde{k}_i/\tilde{k}_r$, and thus is closely related to the evanescent character of
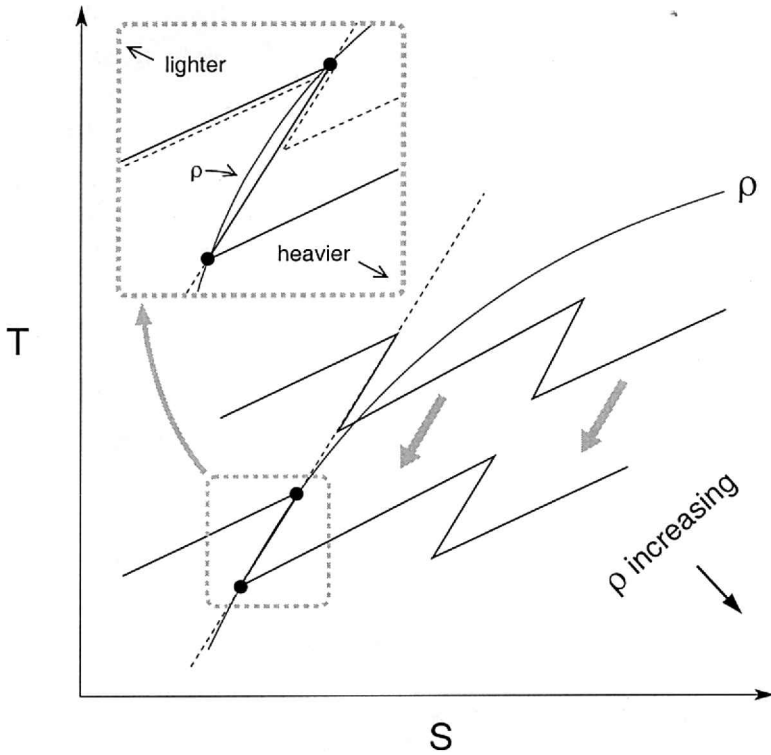
Figure 10. Schematic of an intrusion advancing from warmer to cooler water. Initially the water column is stably stratified at all depths, but at low temperatures the finger-stratified layer may become unstable. The inset gives an expanded view of a finger layer near this critical temperature: top and bottom have the same density, so the layer would be convectively unstable. A similar intrusion with smaller amplitude (dashed curve in inset) would not be unstable.

the solutions. A consequence of this phase-shift is that solutions exhibit recirculating flow between layers (see Figs. 7, 12), so velocities are no longer parallel to phase lines (i.e., interfaces between layers). If the phase-shift is sufficiently large ($>90°$), the "polarity" of the intrusions changes—upward moving parcels will (on average) move right, opposite to the slope of phase lines.

The phase-shift between horizontal and vertical velocities causes the intrusions to migrate vertically. The propagation mechanism is similar to that for linear gravity waves, where propagation occurs because u and w are 90 degrees out of phase. In the present case u and w are nearly in phase, but the slight phase mis-match leads to propagation. The physical mechanism is illustrated in Figure 12b: weak vertical convergences and divergences associated with the out-of-phase component of vertical velocity advect the basic-state and induce vertical propagation. The left-most two profiles show the basic-state and perturbation temperature fields, and the third shows the vertical velocity (shifted
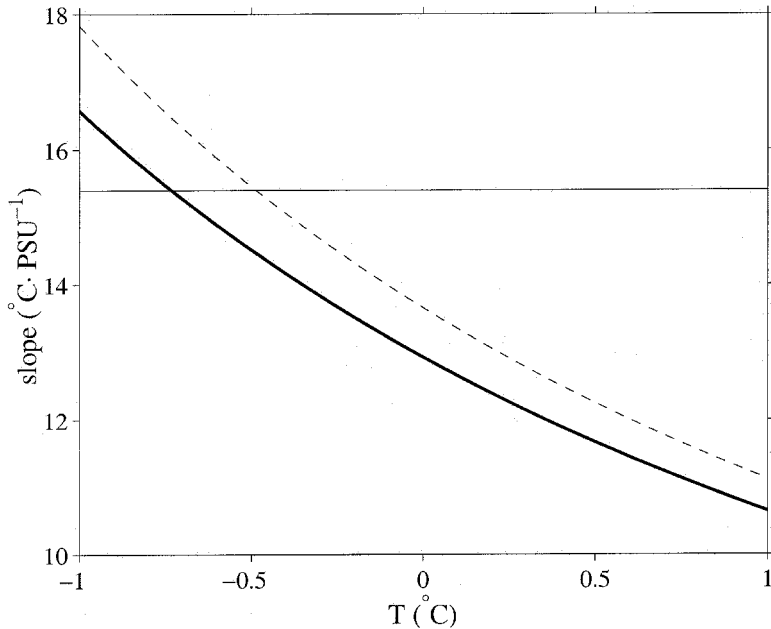
Figure 11. Variation of slope of density lines in the *T-S* plane with temperature, for $S = 34.85$ PSU and $P = 300$ dbar (solid curve). The dashed curve shows the first-order correction due to nonlinearity of the equation of state for an intrusion with peak-to-peak amplitude of $T' = 0.5°C$. The horizontal line at $y = 15.4$ corresponds to the mean slope of the dashed lines shown in Figure 3a. Intersections represent temperatures at which these lines become parallel to density lines, possibly limiting intrusion growth.

downward as a result of spatial trapping). The fourth profile shows the effect on the temperature (according to the linear kinematic wave equation $T_t \approx -w\bar{T}_z$), and the right-most profile shows the resulting vertical phase propagation. The simple propagation mechanism illustrated in the figure is not inherently linked to the α-trapping mechanism discussed previously, and should therefore apply to any trapped interleaving feature. The propagation mechanism can be summarized in physical terms as follows: (1) a nonuniform thermal expansion coefficient α causes intrusions to have spatially decaying amplitude, (2) continuity requires a recirculating flow between interleaving layers, and (3) this recirculating flow induces a phase-shift between horizontal and vertical velocity components, which, through advection of basic-state fields, causes wave-like propagation (Fig. 12).

To explore the character of the vertical propagation, we investigate how growth rates are affected by gradients in α. It will be shown that nonuniform α leads to exponentially growing solutions with complex growth rates, and that in this case the fastest-growing intrusions are propagating features. Complex growth rates were found in studies by Toole and Georgi (1981) and others, but never corresponding to the fastest-growing instability. Rearranging (16) gives a polynomial expression for the growth rate $\tilde{\lambda}$

(a)

(b)
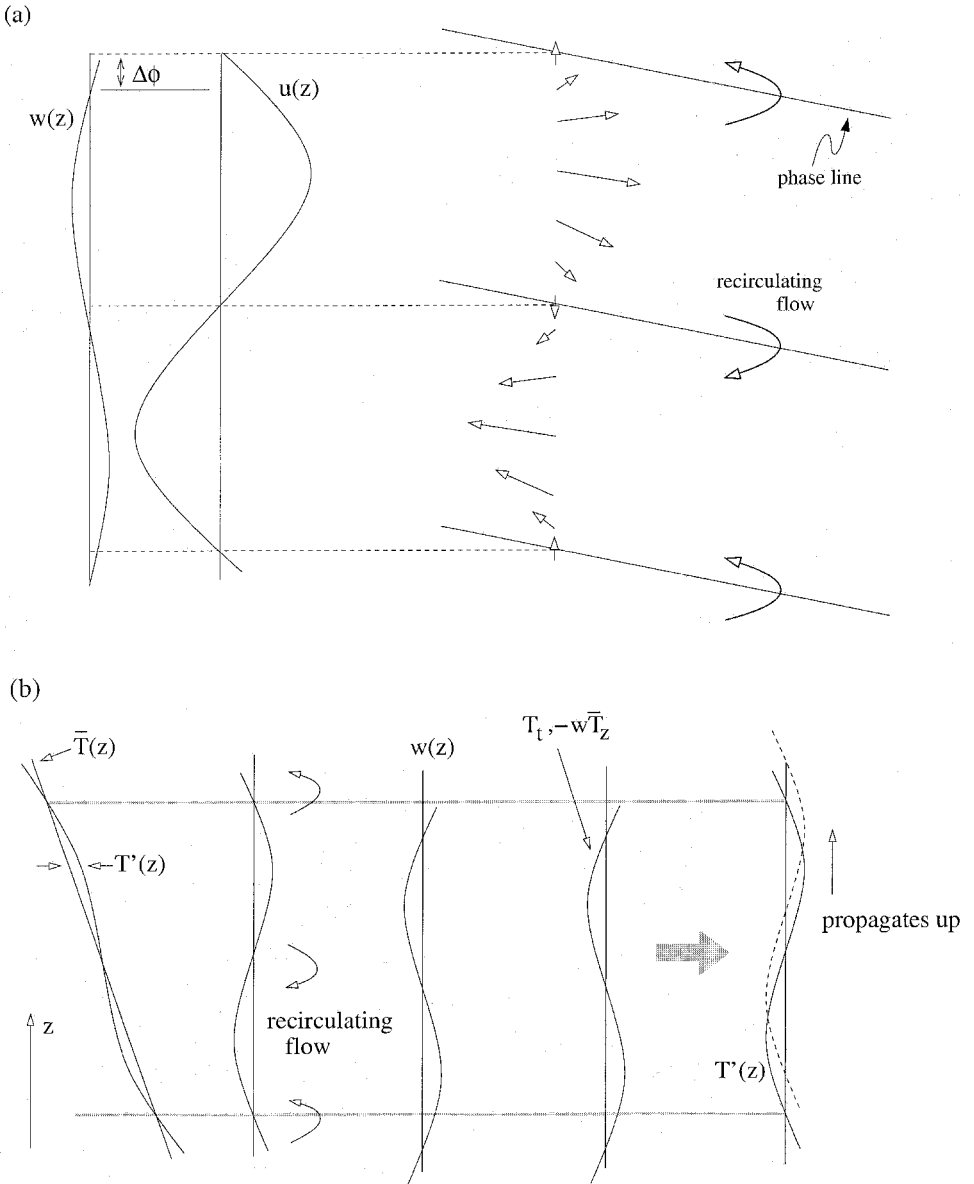

Figure 12. (a) Profiles of u and w, illustrating a vertical phase-shift and the resulting effect on velocities. A recirculating flow between layers occurs, the strength of which is proportional to the phase-shift. (b) Linear wave propagation mechanism which causes intrusions to move vertically: anomalous vertical velocities advect basic-state gradients, causing upward propagation.

$$a\tilde{\lambda}^2 + b\tilde{\lambda} + c = 0$$

$$a = Pr\tilde{m}^2$$

$$b = Pr\tilde{m}^4 + \frac{1}{\tilde{m}^2}(\tilde{k}\tilde{T}_z - \tilde{m}\tilde{T}_x)(\tilde{k} - i\tilde{\alpha}_x) - \frac{\tilde{k}}{\tilde{m}^2}(\tilde{k}\tilde{S}_z - \tilde{m}\tilde{S}_x) \tag{20}$$

$$c = -\tilde{k}(\tilde{k}\tilde{S}_z - \tilde{m}\tilde{S}_x - \gamma_d(\tilde{k}\tilde{T}_z - \tilde{m}\tilde{T}_x)),$$

which is contoured in Figure 13 as a function of $\tilde{m}$ and $\tilde{k}$. The left panel shows the real part and the right panel the imaginary part of the growth rate. Growing intrusions have positive real parts (solid contours); maxima show the location of the fastest-growing intrusion in phase space. The upper panels show the unstable root for the case $\tilde{\alpha}_x = 0$; the lower panels show the case $\tilde{\alpha}_x \neq 0$. Notice that in the nonevanescent case growing solutions have purely real growth rates, whereas in the evanescent case they are complex. This suggests evanescent intrusions are propagating features, while growing non-evanescent intrusions are stationary. This can be demonstrated by considering the marginal stability properties of the solutions. Setting $\tilde{\lambda} = 0$ in (20) gives the marginal stability condition:

$$\tilde{k}(\tilde{k}\tilde{S}_z - \tilde{m}\tilde{S}_x - \gamma_d(\tilde{k}\tilde{T}_z - \tilde{m}\tilde{T}_x)) = 0. \tag{21}$$

If $\tilde{k}$ is real, (21) has solutions $\tilde{k} = 0$ or $\tilde{k} = \tilde{m}(\tilde{S}_x - \gamma_d\tilde{T}_x)/(\tilde{S}_z - \gamma_d\tilde{T}_z)$, implying steady (nongrowing) solutions exist for these values of $\tilde{k}$. If $\tilde{k}$ is complex, as for evanescent solutions, then the only values of $\tilde{k}$ satisfying (21) are the trivial solution $\tilde{k}_r = \tilde{k}_i = 0$ (i.e., a solution with no x-dependence), and the solution defined by the joint conditions $\tilde{k}_r = \tilde{m}(\tilde{S}_x - \gamma_d\tilde{T}_x)/(\tilde{S}_z - \gamma_d\tilde{T}_z)$ and $\tilde{S}_z/\tilde{T}_z = \gamma_d$. The last condition cannot be realized, since $\gamma_d < 1$, while $\tilde{S}_z/\tilde{T}_z > 1$ for a diffusive-sense stratification. Therefore, $\tilde{\lambda}$ cannot vanish for evanescent solutions, and it follows that no marginally stable solutions exist. This suggests that a point-by-point steady-state balance between friction and buoyancy forces (e.g., Walsh and Ruddick, 1998) cannot occur in the evanescent case, and it follows that evanescent intrusions are inherently time-dependent features. These considerations suggest solutions to (11) have the general form:

$$(\psi, S, T) \sim e^{\tilde{\lambda}_r \tilde{t} - \tilde{k}_i \tilde{x}} \sin(\tilde{k}_r \tilde{x} + \tilde{m}\tilde{z} + \tilde{\lambda}_i \tilde{t}). \tag{22}$$

representing propagating disturbances which decay with x. It should be noted that (22) represents a wave propagating in both the x and z directions. However, because oceanic intrusions typically have very small slopes ($\tilde{k}_r \ll \tilde{m}$), the wavenumber vector is nearly vertical, and the phase velocity is also very nearly vertical.

The wavenumber and growth rate for the fastest-growing intrusion are contoured in Figure 14 as functions of $\tilde{k}_i$ and $\tilde{\alpha}_x$. At each point the values of $\tilde{k}_r$ and $\tilde{m}$ which maximize the real part of the growth rate are found, and the corresponding values of $\tilde{\lambda}_i$ and $\tilde{\lambda}_r$ are contoured. Blank regions show areas where the maximization algorithm did not converge, suggesting saddle-point behavior of growth rates, reminiscent of the "UV catastrophe" for
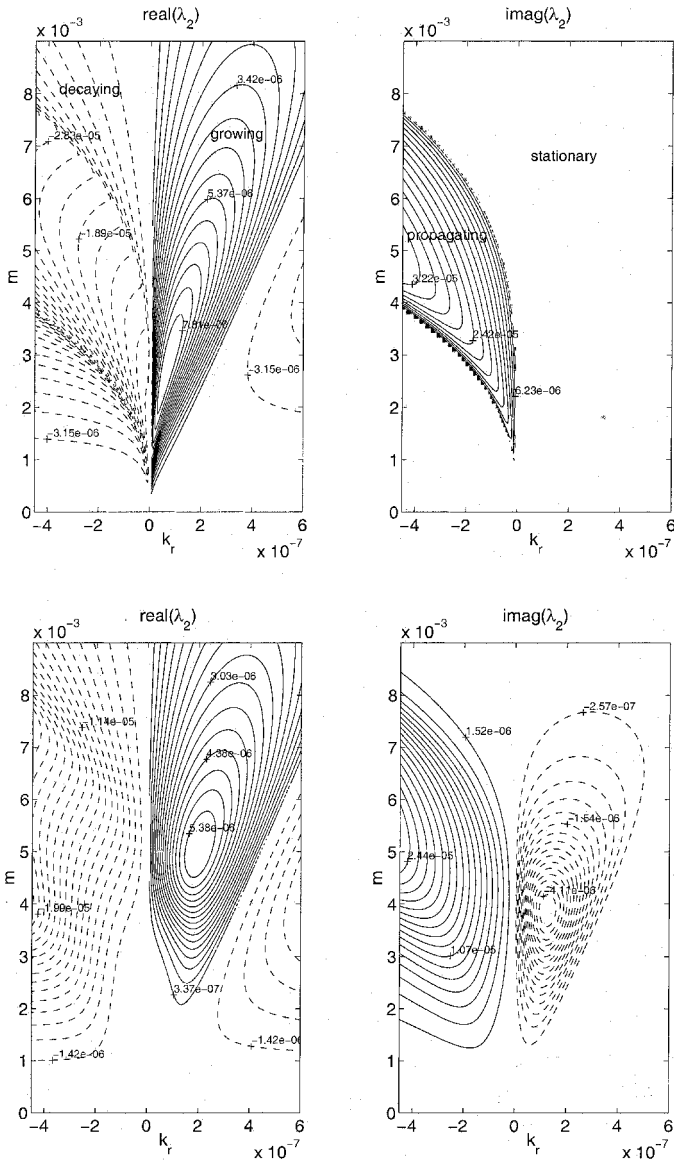
Figure 13. Growth rate plotted as a function of vertical wavenumber $\tilde{m}$ and real part of the horizontal wavenumber ($\tilde{k}_r$) using parameter values from Table 1 (with $\tilde{k}_i = 0$, $\gamma_d = 0.15$, and $Pr = 10$). Dashed contours show negative values. The left and right panels show real and imaginary parts of the growth rate, respectively. Upper panels represent planar, nonevanescent intrusions ($\tilde{\alpha}_x = 0$); lower panels show evanescent roots ($\tilde{\alpha}_x = -1.8 \times 10^{-7}$). Growing, nonevanescent solutions have real growth rates, while evanescent solutions have complex growth rates.
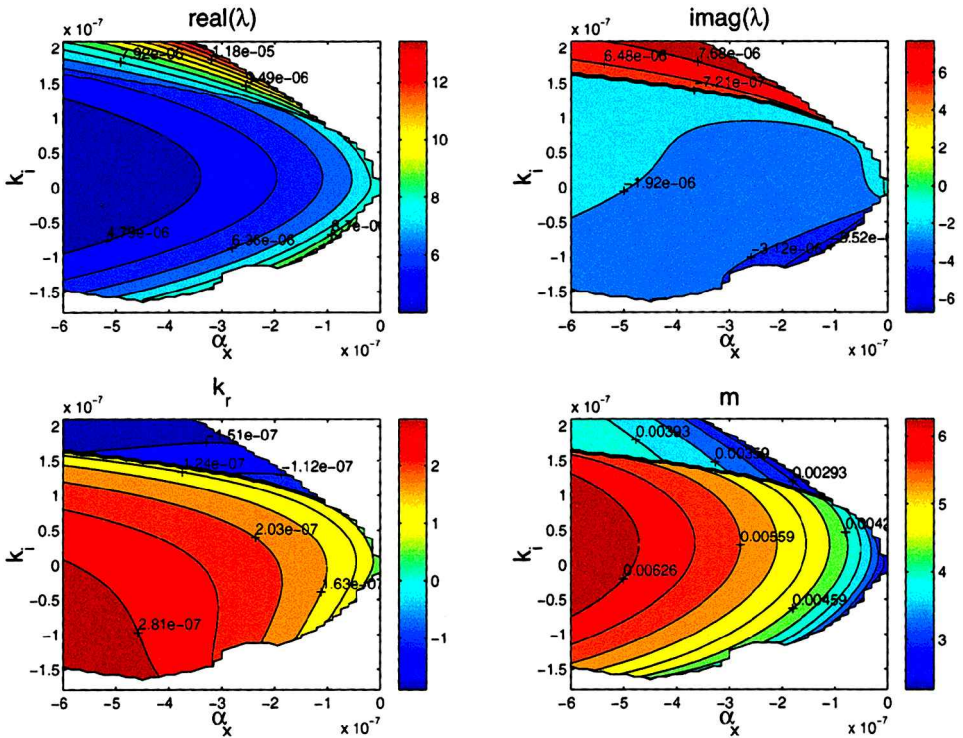
Figure 14. Real and imaginary parts of the growth rate and horizontal and vertical wavenumber for the fastest-growing intrusion, as a function of $\tilde{\alpha}_x$ and $\tilde{k}_i$ (using the parameter values in Table 1, with $\gamma_d = 0.15$ and $Pr = 10$).

intrusion growth rate discussed by Walsh and Ruddick (2000). Solution breakdown occurs outside the region in which the linearized solutions are valid, since neglect of nose-effects requires $\alpha k_i \ll \alpha_x$ (or, nondimensionally, $\tilde{k}_i \ll \tilde{\alpha}_x$), corresponding to a narrow horizontal wedge in the growth rate contour plots.

The phase velocity of solutions is given by $\tilde{\lambda}_r / \tilde{m}$, and this generally increases with $\tilde{k}_i$, so more strongly trapped intrusions propagate faster. Over most of the domain the intrusion behavior is as expected: warm and salty intrusions descend as they cross the front (since $\tilde{k}_r$ and $\tilde{m}$ have the same sign) and the phase velocity is upward. However, for large values of $\tilde{k}_i$ (i.e. strongly evanescent solutions) the behavior changes qualitatively, with warm and salty intrusions *rising* across the front, and intrusions propagating *downward*. This behavior seems inconsistent with diffusive fluxes driving the intrusions, since diffusive convection should tend to make warm intrusions heavy. However, it is reminiscent of the overstable oscillations noted by Toole and Georgi (1981), Walsh and Ruddick (1995), and others. These authors found exponentially growing, oscillatory solutions sloping the "wrong way," but growth rates for these oscillatory modes were found to be smaller than

those for direct (nonoscillatory) modes. We speculate that evanescence damps the different modes unequally, favoring oscillatory behavior for strongly trapped intrusions.

An estimate of the propagation speed of the intrusions may be obtained from Figure 13. The plot suggests a maximum vertical translation of $O(30\text{ m})$ over a one-year period, implying a transit time of roughly 200 m/$(\lambda_*/m_*) \approx$ six years between the Atlantic layer and the surface. For purposes of comparison, the diffusive time-scale is $\tau \sim H^2/K \sim$ $(200\text{ m})^2/3 \times 10^{-5}\,\text{m}^2\text{s}^{-1} \sim 40$ years. The presence of intrusions may affect vertical mixing rates in at least two different ways: first, high-gradient layers associated with intrusions may substantially increase vertical mixing rates (e.g., Kelley, 1984). Second, it is possible that the propagating intrusions produce a significant vertical heat flux by advecting trapped fluid upward, which could further modify effective mixing rates. Vertical shifts may be visible in data, and it would be extremely interesting to attempt to observe the vertical migration directly. Given the crude nature of our model, computed propagation speeds should be considered (at best) qualitative estimates, making observational verification essential.

4. Discussion and conclusions

The T-S structure of intrusions appears to be modified by gradients in α associated with background temperature variations. The idealized analytical model presented here focuses on lateral trapping of intrusions resulting from horizontal variations in α. Solutions exhibit an evanescent character which leads to recirculating flow between layers, and fastest-growing intrusions which propagate, rather than the stationary solutions found in previous studies. Propagation speeds are generally larger for more strongly trapped intrusions. The proposed propagation mechanism is not inherently linked to the α-related trapping mechanism discussed in this work, but should apply to any laterally confined intrusions. If such propagation occurs in the ocean it could have important implications, providing a means of transmitting information between intermediate-depth and near-surface waters. We speculate that vertical migration of intrusions may help explain observations of intrusions in double-diffusively stable regions (e.g., the region immediately beneath the Atlantic layer core, which contains several large intrusions).

The arguments presented in Section 3d suggest that large-amplitude intrusions are inhibited when the lines on which they move through T-S space approach isopycnal slope. The mechanism discussed should apply to both horizontal and vertical trapping of intrusions, and we therefore hypothesize that both may be explained by this mechanism. The trapping mechanism is reminiscent of an idea discussed recently by Merryfield (2000), who proposed that certain large-scale thermohaline staircases may evolve from intrusions. Merryfield speculated that when intrusions spread from their formation region into areas not favorable to growth (e.g., regions with different vertical T-S gradients) they may devolve into staircases, perhaps explaining observations of intrusions surrounded by staircase-like structures (e.g., Meddy Sharon).

Evanescent behavior may affect estimated property fluxes associated with intrusions. The standard empirical method for estimating lateral intrusive fluxes (Joyce, 1977) is based

upon the assumption of a statistical steady-state balance between production of T-S variance by lateral advection and dissipation of variance through mixing. This assumption, along with assumed knowledge of the effective vertical diffusivity, allows a simple expression to be derived for the effective horizontal diffusivity due to interleaving (as discussed in the Introduction). For strongly evanescent intrusions, variance production by lateral advection may be partially balanced by recirculating flow (Figs. 7, 13). This suggests the Joyce model may systematically overestimate lateral fluxes, since the assumption that variance production is entirely balanced by local vertical mixing is incorrect. In fact only a portion of T-S variance is locally dissipated for these evanescent solutions, so the Joyce model may give biased flux estimates.

In Walsh and Ruddick's (1998) study, the planar nature of disturbances meant that along-intrusion density gradients were due solely to background T-S gradients (and therefore could not change). Hence, only vertical gradients could adjust to effect an equilibrium in their model, and they found that intrusions grew until vertical gradients became large enough that small-scale vertical fluxes of T and S balanced lateral advective fluxes. In the present work there is an additional "degree of freedom," since along-intrusion gradients may also evolve due to the evanescent nature of the solutions. We speculate this may offer a new equilibration mechanism, as both the vertical and horizontal decay structure of the intrusions may adjust to achieve an equilibrium. This could lead to coupling of the lateral and vertical structure of intrusions, with each adjusting relative to the other as they evolve toward an equilibrium, and may be an important factor in establishing the "nested" character of the Arctic intrusions (Walsh and Carmack, 2001).

Because our model has no externally imposed length scale it does not predict a specific value for the lateral decay scale, but rather a relationship between $\tilde{\lambda}_i$ and $\tilde{k}_i$ (i.e., between evanescent decay scale and propagation speed). In reality, external scales are always present, and should provide a selection mechanism for the lateral decay scale of intrusions. The estimated decay scale of $\sim$1000 km is significantly larger than the width of Arctic boundary currents. However, we note that this is a very rough estimate, and the real value for the decay scale may be quite different. If the value of $\sim$1000 km is accurate, however, it would suggest that other factors besides those discussed here may be controlling the horizontal extent of the Arctic intrusions.

Many features of intrusions are not well represented in the present model, and these may suggest useful extensions of this work. For example, recirculating flow between interleaving layers may lead to vortex stretching, generating relative vorticity in a rotating system, and possibly affecting the behavior of Arctic intrusions. Also, cabbeling effects may be important when T-S gradients become large, providing an additional driving force for the intrusions. Fluxes through salt-finger layers have been ignored, and these may become important after the intrusions reach large amplitude and finger-stratified layers form. These issues are beyond the scope of the present study, and are the subject of on-going investigations.

APPENDIX

WKB solution

A more complete picture of the spatial structure of the intrusions can be obtained via WKB analysis of (13). The coefficients in (13) are slowly varying functions of x, so approximate techniques can be used to find the asymptotic behavior of solutions in the high-wavenumber limit. The approximation will be valid when the wavelength is much shorter than the scale on which background property variations occur (i.e., when P and Q, defined as in (13), vary only slightly over a wavelength). The WKB solution to (13) is of the form

$$\hat{\psi} = \text{Re}(A(x)e^{i\phi(x)}). \tag{23}$$

where $\phi(x)$ and $A(x)$ are slowly varying, real-valued phase and amplitude functions. Substituting into (13) gives the following pair of equations for the phase and amplitude

$$A' \, \text{Re}(P) \approx A(\phi'^2 + \text{Im}(P)\phi' - \text{Re}(Q))$$
$$(2\phi' + \text{Im}(P))[\phi'^2 + \phi' \, \text{Im}(P) - \text{Re}(Q)] + \text{Re}(P)[\text{Im}(Q) + \phi' \, \text{Re}(P)] = 0, \tag{24}$$

where primes ($'$) denote derivatives, and, consistent with the WKB approximation, terms containing second derivatives of ϕ and A have been dropped. If we now identify ϕ' with the horizontal wavenumber (denoted by k), (24b) becomes a polynomial equation for the wavenumber

$$(2k + \text{Im}(P))[k^2 + \text{Im}(P)k - \text{Re}(Q)] + \text{Re}(P)[\text{Im}(Q) + \text{Re}(P)k] = 0. \tag{25}$$

(Notice this is a cubic equation for the real part of the wavenumber, while (13) shows that the complex wavenumber satisfies a simpler quadratic equation.) Once k is known, (24a) may be used to compute $A(x)$:

$$A(x) \approx c_0 e^{\int \text{Re}(P)^{-1}[k^2 + \text{Im}(P)k - \text{Re}(Q)]dx} \tag{26}$$

If P and Q are constants, and if k can be considered locally constant, then $A(x)$ has exponential form

$$A(x) \approx c_0 e^{\sigma x} \tag{27}$$

$$\sigma \equiv \text{Re}(P)^{-1}[k^2 + \text{Im}(P)k - \text{Re}(Q)].$$

In this case the solutions reduce to the limiting case considered in section 3c, and solutions to (13) are of the form:

$$\hat{\psi} \sim \text{Re}(e^{(\sigma + ik)x}). \tag{28}$$

Keeping the weak x-dependence of the coefficients P and Q leads to a more complicated amplitude function than (27), which may be computed in a straightforward manner from (26).

REFERENCES

Anderson, L. G., E. P. Jones, K. P. Koltermann, P. Schlosser, J. H. Swift and D. W. R. Wallace. 1989. The first oceanographic section across the Nansen Basin in the Arctic Ocean. Deep-Sea Res., *36,* 475–482.

Carmack, E. C., K. Aagaard, J. H. Swift, R. W. Macdonald, F. A. McLaughlin, E. P. Jones, R. G. Perkin, J. N. Smith, K. M. Ellis and L. R. Killius. 1997. Changes in temperature and tracer distributions within the Arctic Ocean: results from the 1994 Arctic Ocean section. Deep-Sea Res. II, *44,* 1487–1502.

Carmack, E. C., K. Aagaard, J. H. Swift, R. G. Perkin, F. A. McLaughlin, R. W. Macdonald and E. P. Jones. 1998. Thermohaline transitions, *in* Physical Processes in Lakes and Oceans, J. Imberger, ed., Amer. Geophys. Union, Coastal and Estuarine Studies, *54,* 179–186.

Carmack, E. C., R. W. Macdonald, R. G. Perkin, F. A. McLaughlin and R. J. Pearson. 1995. Evidence for warming of Atlantic water in the southern Canadian Basin of the Arctic Ocean: results from the Larsen-93 expedition. Geophys. Res. Lett., *22,* 1061–1064.

Fine, R. A., C. N. K. Mooers and F. J. Millero. 1978. Effects of nonlinear pressure-volume-temperature properties on the potential energy distribution in the Atlantic Ocean. Deep-Sea Res., *25,* 15–22.

Fofonoff, N. P. 1961. Energy transformations in the sea, (unpublished manuscript) Fisheries Res. Bd., Report Series 109, Canada, 82 pp.

——— 1998. Nonlinear limits to ocean thermal structure. J. Mar. Res., *56,* 793–811.

Freeland, H. J., P. B. Rhines and T. Rossby. 1975. Statistical observations of the trajectories of neutrally buoyant floats in the North Atlantic. J. Mar. Res., *33,* 383–404.

Gill, A. E. 1973. Circulation and bottom water production in the Weddell Sea. Deep-Sea Res., *20,* 111–140.

Hamon, B. V. 1967. Medium-scale temperature and salinity structure in the upper 1500 m in the Indian Ocean. Deep-Sea Res., *14,* 169–181.

Iselin, C. O'D. 1939. The influence of vertical and lateral turbulence on the characteristics of the waters at mid-depths. Trans. Amer. Geophys. Union, *20,* 414–417.

Joyce, T. M. 1977. A note on the lateral mixing of water masses. J. Phys. Oceanogr., *7,* 626–629.

Kelley, D. 1984. Effective diffusivities within oceanic thermohaline staircases. J. Geophys. Res., *89,* 10484–10488.

Kuz'mina, N. P. and V. B. Rodionov. 1992. Influence of baroclinicity on formation of thermohaline intrusions in ocean frontal zones. Izvestiya, Atmospheric and Oceanic Physics, *28,* 804–810.

Kuz'mina, N. P. and V. Zhurbas. 2000. Effects of double-diffusion and turbulence on interleaving at baroclinic oceanic fronts. J. Phys. Oceanogr., *30,* 3025–3038.

May, B. D. and D. E. Kelley. 1997. Effect of baroclinicity on double-diffusive interleaving. J. Phys. Oceanogr., *27,* 1997–2008.

McDougall, T. J. 1985. Double-diffusive interleaving. Part I: linear stability analysis. J. Phys. Oceanogr., *15,* 1532–1541.

Merryfield, W. J. 2000. Origin of thermohaline staircases. J. Phys. Oceanogr., *30,* 1046–1068.

Niino, H. 1986. A linear stability theory of double-diffusive horizontal intrusions in a temperature-salinity front. J. Fluid Mech., *171,* 71–100.

Perkin, R. G. and E. L. Lewis. 1984. Mixing in the West Spitsbergen Current. J. Phys. Oceanogr., *14,* 1315–1325.

Quadfasel, D., A. Sy and B. Rudels. 1993. A ship of opportunity section to the North Pole: upper ocean temperature observations. Deep-Sea Res., *40,* 777–789.

Richards, K. J. 1991. Double-diffusive interleaving at the Equator. J. Phys. Oceanogr., *21,* 933–938.

Rothrock, D. A., Y. Yu and G. A. Maykut. 1999. Thinning of the Arctic sea-ice cover. Geophys. Res. Lett., *26,* 3469–3472.

Ruddick, B. R. and D. Hebert. 1988. The mixing of Meddy "Sharon," *in* Small-Scale Mixing in the Ocean, J. C. J. Nihoul and B. M. Jamart, eds., Elsevier Oceanogr. Ser., *46,* 249–262.

Ruddick, B. R. and J. S. Turner. 1979. The vertical length scale of double-diffusive intrusions. Deep-Sea Res., *26,* 903–913.

Rudels, B., G. Björk, R. D. Muench and U. Schauer. 1999. Double-diffusive layering in the Eurasian Basin of the Arctic Ocean. J. Mar. Syst., *21,* 3–27.

Rudels, B., E. P. Jones, L. G. Anderson and G. Kattner. 1994. On the intermediate depth waters of the Arctic Ocean, *in* The Polar Oceans and Their Role in Shaping the Global Environment, Geophys. Monogr., *85,* Amer. Geophys. Union, 33–46.

Smethie, W. M., Jr., P. Schlosser and G. Bönisch. 2000. Renewal and circulation of intermediate waters in the Canadian Basin observed on the SCICEX '96 cruise. J. Geophys. Res., *105,* 1105–1121.

Steele, M. and T. Boyd. 1998. Retreat of the cold halocline layer in the Arctic Ocean. J. Geophys. Res., *103,* 10419–10435.

Stern, M. E. 1967. Lateral mixing of water masses. Deep-Sea Res., *14,* 747–753.

Stommel, H. and N. K. Fedorov. 1967. Small scale structure in temperature and salinity near Timor and Mindinao. Tellus, *19,* 306–325.

Swift, J. H., E. P. Jones, K. Aagaard, E. C. Carmack, M. Hingston, R. W. Macdonald, F. A. McLaughlin and R. G. Perkin. 1997. Waters of the Makarov and Canadian basins. Deep-Sea Res. II, *44,* 1503–1529.

Toole, J. M. and D. T. Georgi. 1981. On the dynamics and effects of double-diffusively driven intrusions. Progr. Oceanogr., *10,* 121–145.

Turner, J. S. 1965. The coupled turbulent transports of salt and heat across a sharp density interface. Int. J. Heat and Mass., *8,* 759–767.

Walsh, D. and E. Carmack. 2001. Nested character of Arctic thermohaline intrusions, *in* Proceedings of the Sixth Conference on Polar Meteorology and Oceanography (May 14–18, 2001), published by the American Meteorological Society, 113–116.

Walsh, D. and B. Ruddick. 1995. Double-diffusive interleaving: The influence of nonconstant diffusivities. J. Phys. Oceanogr., *25,* 348–358.

—— 1998. Nonlinear equilibration of thermohaline intrusions. J. Phys. Oceanogr., *28,* 1043–1070.

—— 2000. Double-diffusive interleaving in the presence of turbulence—the effect of a non-constant flux ratio. J. Phys. Oceanogr., *30,* 2231–2245.

Zhurbas, V. M., N. P. Kuz'mina and I. D. Lozovatskiy. 1988. The role of baroclinicity in intrusive layering in the ocean. Oceanology, *28,* 34–36.